



Comparison of dynamic deformation using electromagnetic hydraulic forming and electromagnetic forming

Peng Zhao¹ · Ziqin Yan¹ · Xiaohui Cui^{1,2,3}

Received: 31 August 2021 / Accepted: 14 December 2021 / Published online: 28 January 2022
© The Author(s), under exclusive licence to Springer-Verlag London Ltd., part of Springer Nature 2021

Abstract

This paper proposes a new sheet forming method that combines electromagnetic forming (EMF) with hydraulic forming called electromagnetic hydroforming (EMHF). Finite element models of both the EMF and EMHF processes were established using ANSYS and ABAQUS. Then, dynamic free bulging deformation of 5052 aluminum alloy during the forming processes was analyzed. The EMF process results in a deformed sheet profile with an uneven conical shape, whereas EMHF leads to a deformed profile with a regular circular shape. This is because during the EMHF process, electromagnetic impact energy is transformed into liquid pressure that is evenly distributed on the sheet surface. When the discharge voltage is 4.5 kV, the maximum deformation speed and strain rate reached 70.6 m/s and 2176.8 s⁻¹, respectively. Thus, EMHF can be considered a high-speed forming method. The simulation results for both EMF and EMHF were verified by experiment at two different discharge voltages. The maximum error was less than 7.4%.

Keywords Electromagnetic forming · Hydraulic forming · Finite element simulation · Deformation behavior

1 Introduction

Electromagnetic forming (EMF) is a high-speed forming process based on the following principle. When a large pulse of current passes through the coil, a strong magnetic field is produced around the coil. As the induced current and magnetic force are simultaneously generated on the metal sheet, the sheet is deformed at high speed. Compared with traditional stamping, EMF can significantly improve the formability of materials and reduce springback of parts. For example, Su et al. [1] found that the forming limit of AA 2219-O sheets is 45.4% higher under electromagnetic tensile loading compared with quasi-static (QS) tensile loading. Li et al. [2] showed that the electromagnetic forces generated on sheet lead to dislocation cross slips and dislocation

cell structures in aluminum alloy. Cui et al. [3] proposed a method of reverse magnetic force loading to reduce springback in V-shaped parts. The springback angle was found to decrease with increasing discharge energy. This is due to higher frequency oscillations (caused by disorder) that appear in the EMF process, which reduces internal stress in parts. Cui et al. [4] proposed an electromagnetic partitioning forming method to realize forming and springback control of large-curvature parts. Du et al. [5] proposed a novel method of electromagnetic partitioning forming with elastic cushion, which can reduce springback by vibrate at high speed under the action of the electromagnetic force and the rebound force of the elastic pad.

At present, electromagnetic tube forming is widely used for tube bulging, tube compression, and tube connection since the electromagnetic force can be uniformly distributed on the tube. Cui et al. [6] obtained a higher bulging height by applying axial magnetic pressure to the tube end during the bulging process. Yu et al. [7] introduced an additional calibration process into single-step EMF to obtain square tubes with small, rounded corners. Yan et al. [8] used a multi-seam field-shaper to solve the problem of uneven welding of steel/aluminum tubes.

EMF technology is also widely used for sheet forming. Cui et al. [9] found that when a planar spiral coil is used

✉ Xiaohui Cui
cuixh622@csu.edu.cn

¹ College of Mechanical and Electrical Engineering, Central South University, Changsha 410083, China
² Light Alloy Research Institute, Central South University, Changsha 410083, China
³ State Key Laboratory of High Performance Complex Manufacturing, Central South University, Changsha 410083, People's Republic of China

in electromagnetic sheet forming, the electromagnetic force on the sheet material is “M” shaped. The electromagnetic force is close to zero at the sheet center and maximum at middle turns of the coil. Xiong et al. [10] carried out a series of EMF V-bending experiments with rectangular samples. Inhomogeneous deformation appears along sheet width direction due to the non-uniform electromagnetic force on the sheet. Xu et al. [11] analyzed the effect of an aluminum drive plate on electromagnetic bulging of AZ31 magnesium alloy. The material formability was improved when a driver sheet with a thickness 1 mm was used. The high strain rate led to grain refinement and the appearance of twins in the magnesium alloy. Huang et al. [12] proposed a novel method named current-assisted electromagnetic forming, which can improve the plastic deformation effect of metals.

To improve geometric accuracy in sheet forming, Vohnout [13] proposed electromagnetic-assisted stamping (EMAS) and realized precise manufacture of car doors. The EMAS process involves both quasi-static preforming and local dynamic high-speed forming. Kiliçlar et al. [14] increased the material forming limit by modifying the strain rate and strain paths in EMAS. Liu et al. [15] used EMAS to manufacture cylindrical parts, which solved the problem that cylindrical parts with a corner radius break easily during the traditional drawing process. Cui et al. [16] used multi-directional magnetic pressure to reduce the corner radius of cylindrical parts manufactured by deep drawing. After stamping, coils for bulging and radial pushing were placed at the rounded corners and sheet end. The material fluidity was improved and maximum increase in thickness at the sheet rounded corners was achieved when coils were used for radial pushing, compared with only coils for bulging. However, the coil must be set inside the mold in EMAS, which is difficult and increases the mold and coil production costs. Moreover, the service life of the mold and coil are sharply reduced, resulting in EMAS processes that are not suitable for industrial application.

In this paper, an electromagnetic hydroforming (EMHF) that combines EMF with hydraulic forming (HF) is proposed. The deformation behavior of 5052 aluminum alloy sheets under both EMHF and EMF were analyzed through experiment and numerical simulations.

2 Materials and experimental procedure

Figure 1a illustrates the EMHF system (1/4 model) used in the experiment. The coil had a planar helical structure, consisting of 13 turns of copper wire. The cross section of the copper wire was 3 mm × 10 mm and the distance between each wire was 1.4 mm. The diameter and thickness of the drive plate were 135 mm and 3 mm, respectively. The punch was located above the drive plate and formed an enclosed

space between the water chamber and sheet, which was filled with water. A 5052 aluminum alloy sheet with a thickness of 0.5 mm was then placed between the die and water chamber for forming. During the EMHF process, the pulse current flowed through the coil and generated a strong magnetic force on the drive plate. The water and punch were driven away from the coil by the drive plate. Finally, the sheet was deformed. A schematic diagram of the EMF system (1/4 model) is shown in Fig. 1b. The coil, sheet, and die were identical to those used in the EMHF system. Figure 1c shows the measured current flowing through the coil at various discharge voltages.

Figure 2 shows a representative stress–strain curve of 5052 aluminum alloy sheet obtained under quasi-static conditions using a tensile testing machine. To consider the effect of strain rate on the forming process, the Cowper-Symonds constitutive model was adopted. Cui et al. [3] and Feng et al. [17] have accurately predicted the electromagnetic forming process of 5052 aluminum alloy using C-S constitutive model. For 5052 aluminum alloy, $C = 6500 \text{ s}^{-1}$ and $P = 0.25$ [3, 17].

$$\sigma = \sigma_y \left[1 + \left(\frac{\dot{\epsilon}}{C} \right)^P \right] \quad (1)$$

where σ is the dynamic flow stress, σ_y is the true stress in the quasi-static state, and $\dot{\epsilon}$ is the plastic strain rate.

Figure 3 shows the sheet deformation results of the two forming methods. With EMHF, the forming height was 17.7 mm and 21.7 mm at discharge voltages of 4 kV and 4.5 kV, respectively. When the discharge voltage was 5 kV, cracking occurred on the top of the sheet. With EMF, the forming height was 18.1 mm, 19.9 mm, and 22.5 mm at discharge voltages of 4 kV, 4.5 kV, and 5 kV, respectively. When the voltage was increased from 4 to 4.5 kV, the forming height increased by 22.6% and 9.9% in the EMHF and EMF processes, respectively. The deformed sheet profiles were regular circular and uneven irregular cone, respectively.

3 Numerical modeling and simulations

A flowchart of the numerical simulation of the EMHF process is illustrated in Fig. 4. During each time step, the transient magnetic forces generated on the drive plate were obtained using the ANSYS/Emag software. The magnetic forces were imported into the ABAQUS/Explicit software. Then the dynamic deformation processes of the drive plate, punch, water, and sheet were simulated. The drive plate was once again imported into ANSYS/Emag and the magnetic forces were calculated based for the next time step on the location of the driver plate. Multiple calculations of

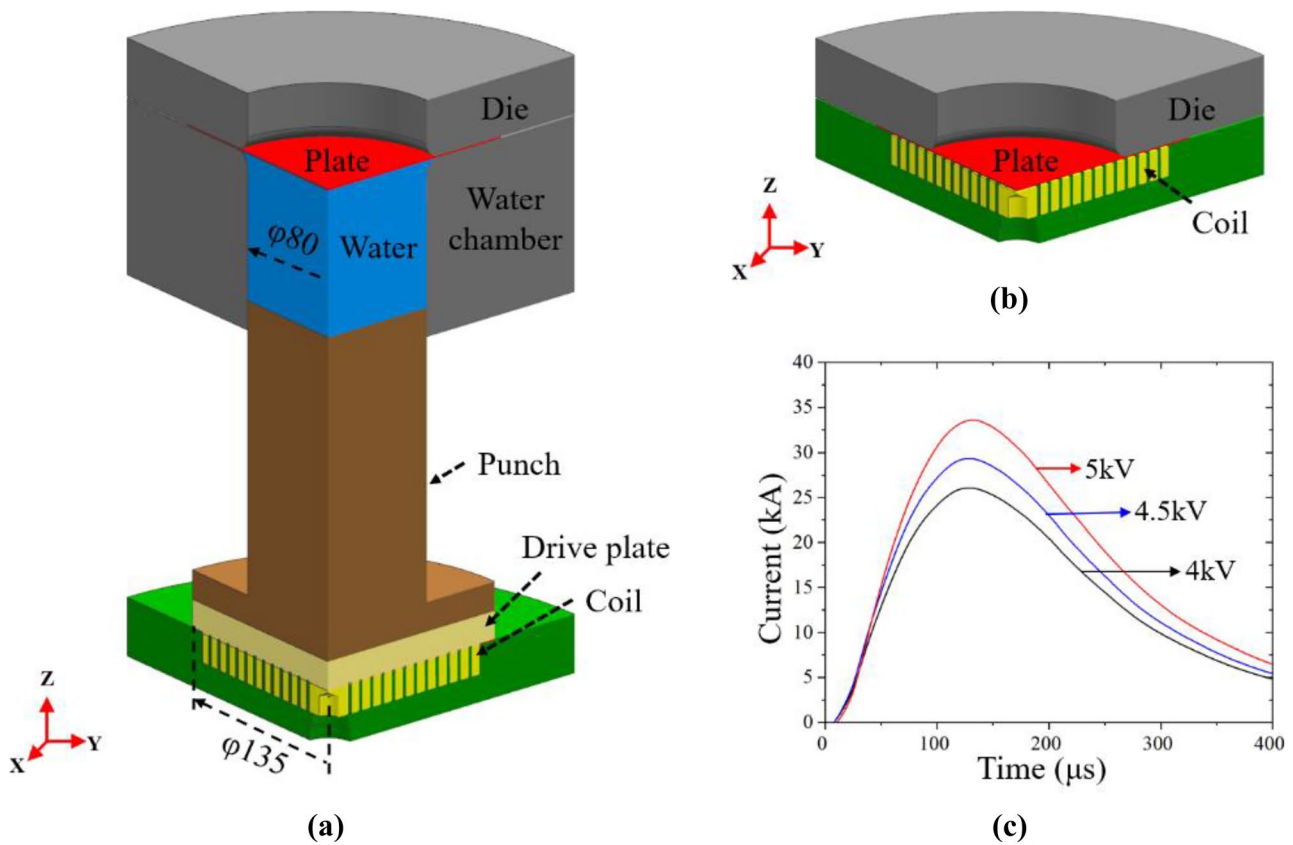


Fig. 1 Schematic illustration of high-rate forming system: (a) EMHF, (b) EMF, and (c) current flowing through the coil at different voltages

magnetic force and dynamic deformation were performed until sheet deformation was complete.

Figure 5 shows a flowchart of numerical simulation process for EMF. As previously, transient magnetic forces generated on the sheet were obtained using the ANSYS/Emag.

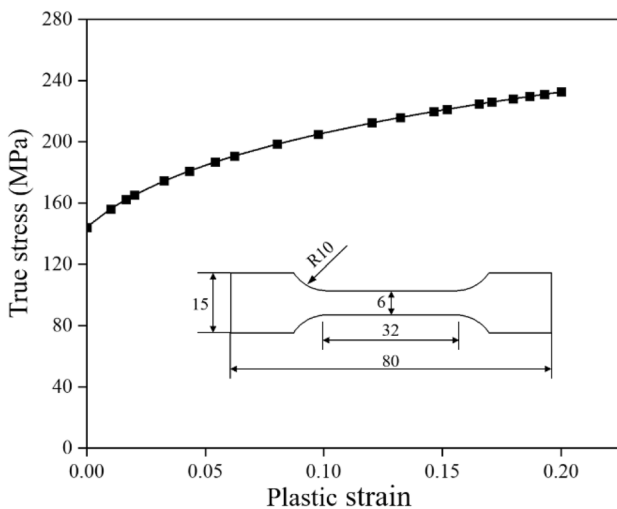


Fig. 2 Stress–strain curve of 5052 aluminum alloy under tensile quasi-static loading

The magnetic force was imported into ABAQUS/Explicit and the sheet deformation was calculated. The deformed sheet was then imported into ANSYS/Emag to calculate the magnetic forces for the next time step. The process was repeated until the sheet deformation was complete.

A three-dimensional electromagnetic field model of the EMHF process was established, as shown in Fig. 6a. The coil and drive plate were sealed in air. The coil and sheet were divided into a hexahedral mesh model, as shown in Fig. 6b. The structured field model of EMHF (1/4 model) is shown in Fig. 6c, including the drive plate, punch, water, sheet, and die. The Lagrange algorithm was used for the sheet material and the Euler algorithm was used for the fluid. The sheet, drive plate, and punch were modeled using the C3D8R solid element. The water and air were modeled using the EC3D8R solid element. Figure 6d shows the structure field model of EMF (1/4 model).

Figure 7 shows volume fraction of air in liquid flow area with a discharge voltage of 4.5 kV. Initially, water fills the water chamber. At 220 μs , the punch is driven upward by the drive plate, which causes the water to move upward and the sheet deforms. As time progresses, the punch continues to push the water upward, as the electromagnetic energy is

Fig. 3 Experimental results: (a) EMHF and (b) EMF

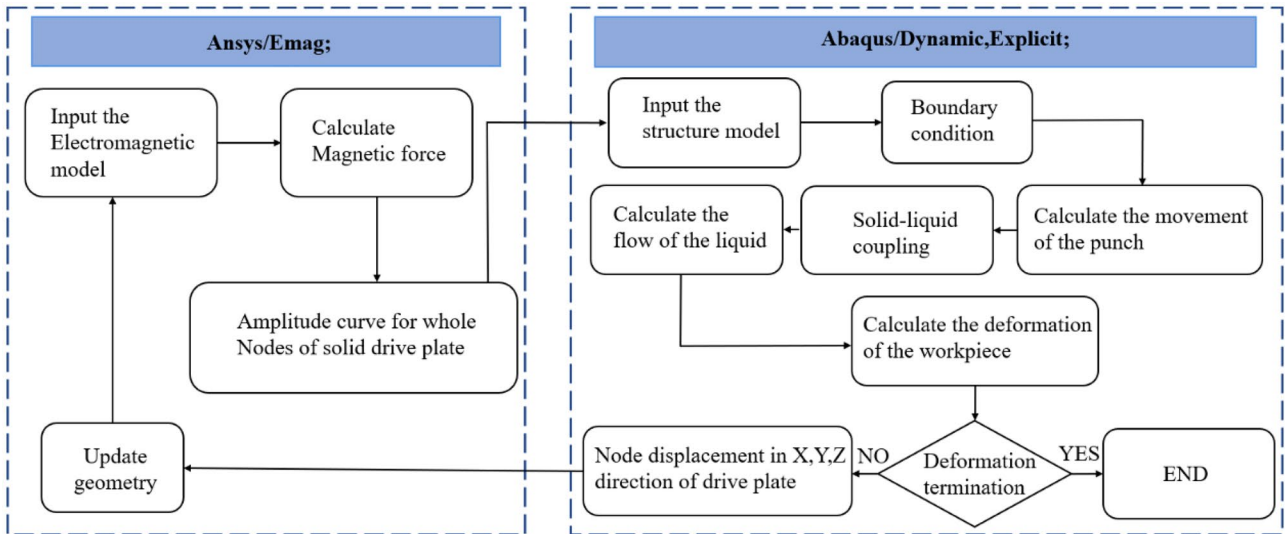
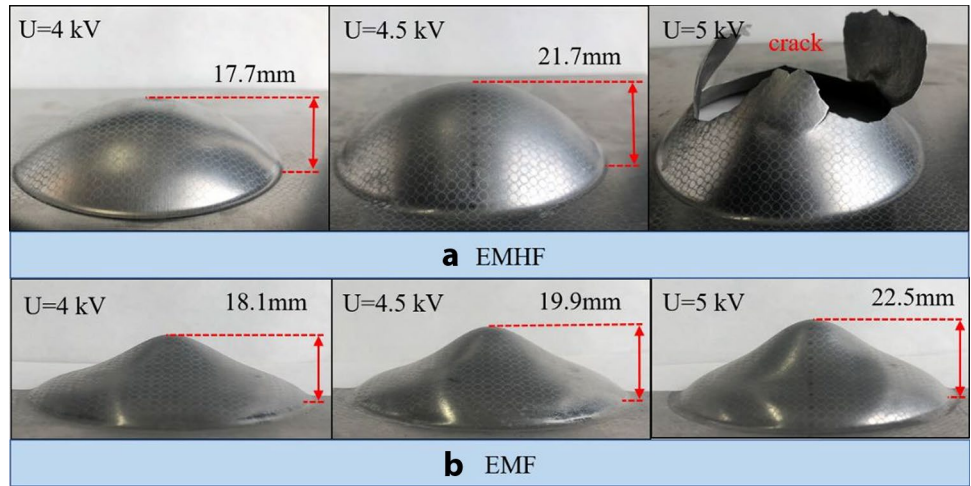


Fig. 4 Flowchart of numerical simulation of EMHF

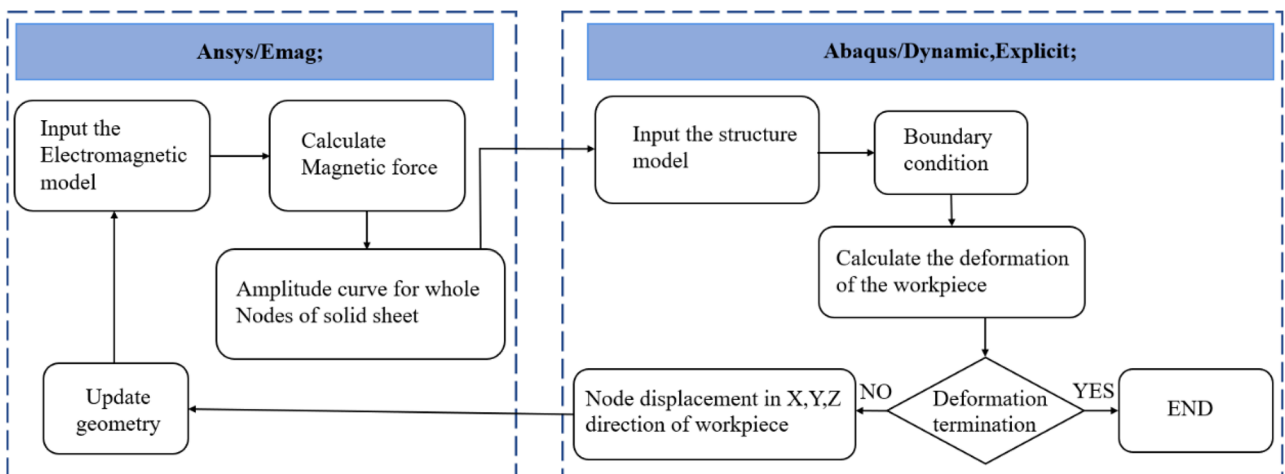


Fig. 5 Flowchart of numerical simulation of EMF

transformed into liquid pressure, which pushes the material outward, evenly in all directions.

Figure 8 shows the velocity of the punch, water, and sheet along the Z-axis during EMHF at a discharge voltage of 4.5 kV. The sheet center is defined as point A and point B is the node 20 mm away from point A. At 220 μs , the velocity of points A and B are 18.3 m/s and 25.1 m/s, respectively. The velocity of the sheet center is smaller than the velocity of the peripheral nodes, resulting in a smaller displacement at the sheet center. The velocity of the sheet center becomes greater than the velocity of the peripheral nodes with increasing time. At 1200 μs , the velocity of points A and B are 1.8 m/s and 4.9 m/s, respectively, and deformation of the sheet is complete.

Figure 9 shows the velocity of the sheet along the Z-axis during EMF at a discharge voltage of 4.5 kV. The diameter portion of the upper surface of the sheet was defined as Path 1. At 60 μs , the velocity of point A is 19.3 m/s and that of point B is 70.1 m/s. At 135 μs , the velocity of point

A is 323.8 m/s and that of point B is 74.9 m/s. At 1000 μs , the velocity of point A is 1.7 m/s and that of point B is 3.8 m/s. Thus, demonstrating a trend toward termination of sheet deformation can be shown.

Figure 10 shows the relationship between the deformation profile and time along Path 1 at a discharge voltage of 4.5 kV. In EMF, the sheet profile is M-shaped from 80 to 120 μs , with large displacement on the sides of sheet and less displacement in the middle. From 120 to 140 μs , the sheet center is accelerated upward by inertial forces and the sheet profile gradually becomes conical. At 1000 μs , displacement of sheet center reaches a maximum and deformation of the sheet is complete. In EMHF, the displacement due to deformation of point A is slightly smaller than that of point B at 400 μs . From 600 to 2000 μs , the sheet profile is characterized as high in the middle and low on both sides. At 2000 μs , smaller displacements occur farther away from the sheet center. The final sheet profile is a uniform semicircle.

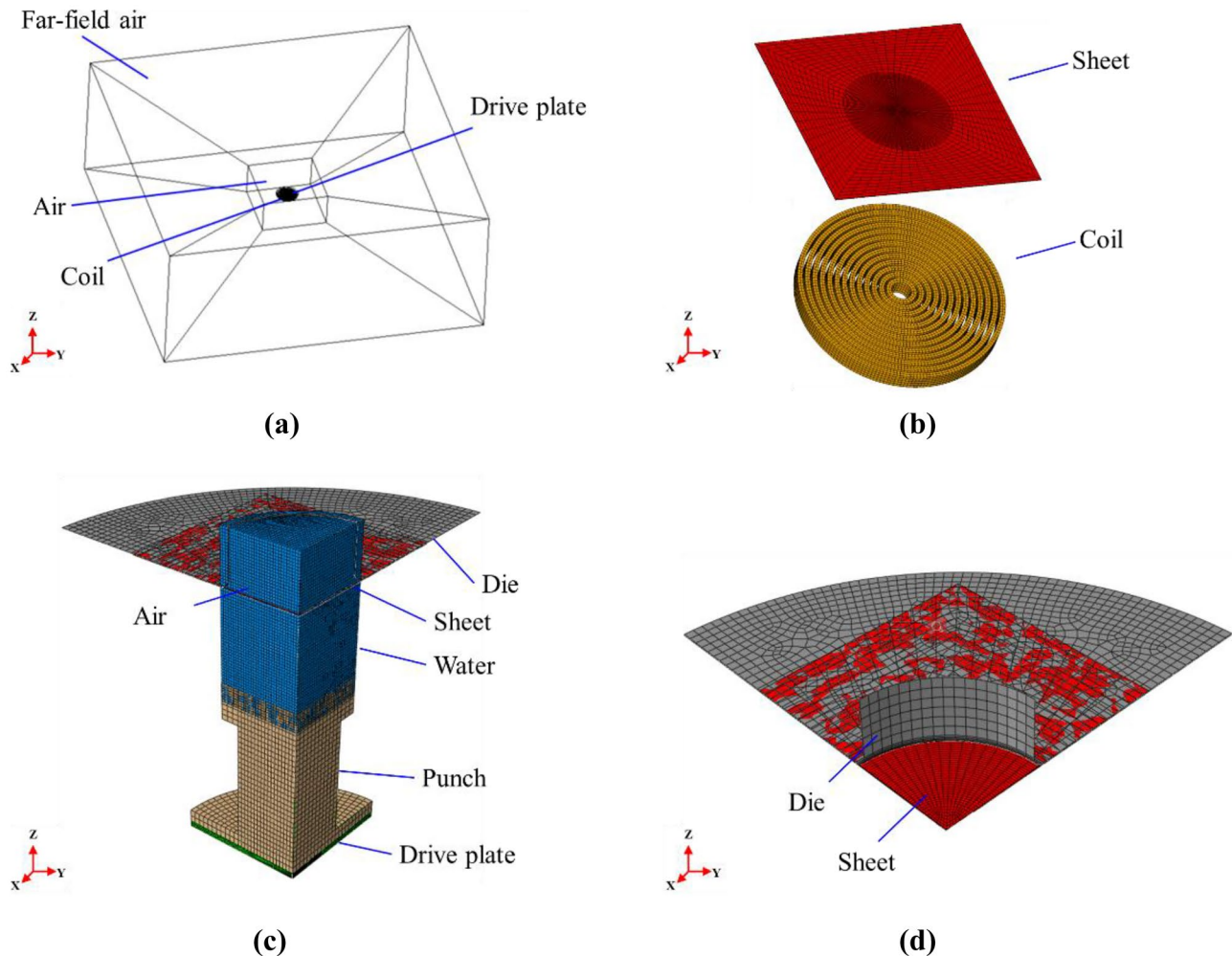


Fig. 6 Finite element modeling: (a) electromagnetic field of EMHF, (b) mesh model of coil and sheet, (c) structured field of EMHF, and (d) structured field of EMF

Fig. 7 Liquid flow during EMHF: (a) $t=0 \mu\text{s}$, (b) $t=220 \mu\text{s}$, (c) $t=430 \mu\text{s}$, and (d) $t=1200 \mu\text{s}$

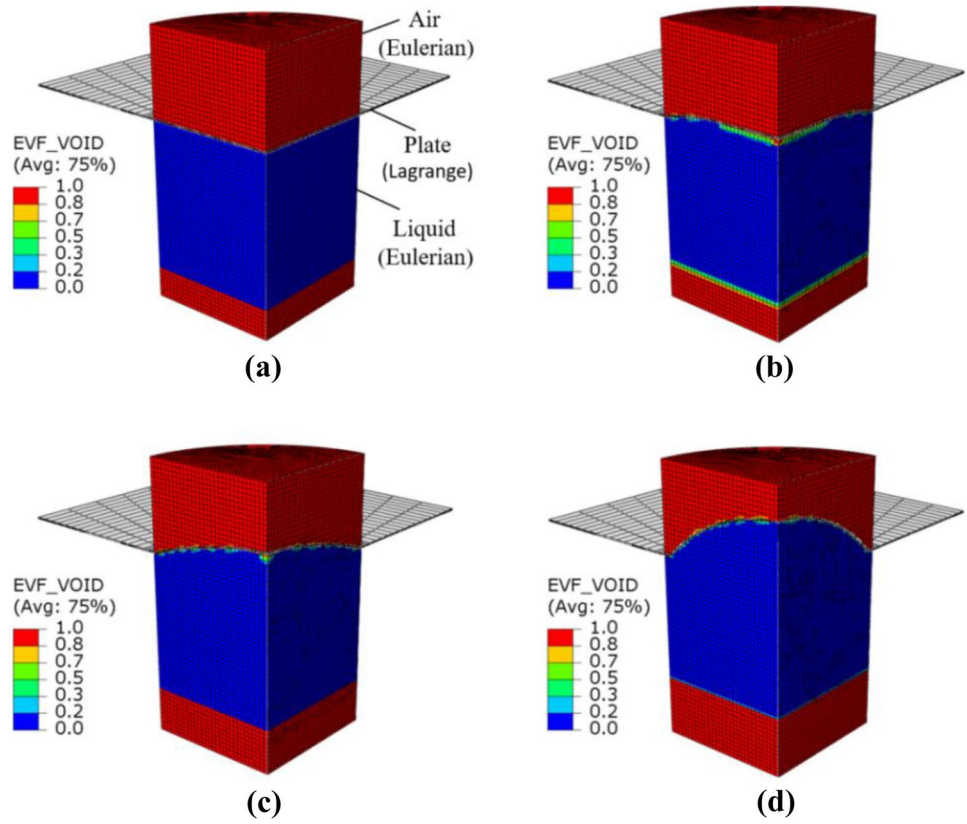
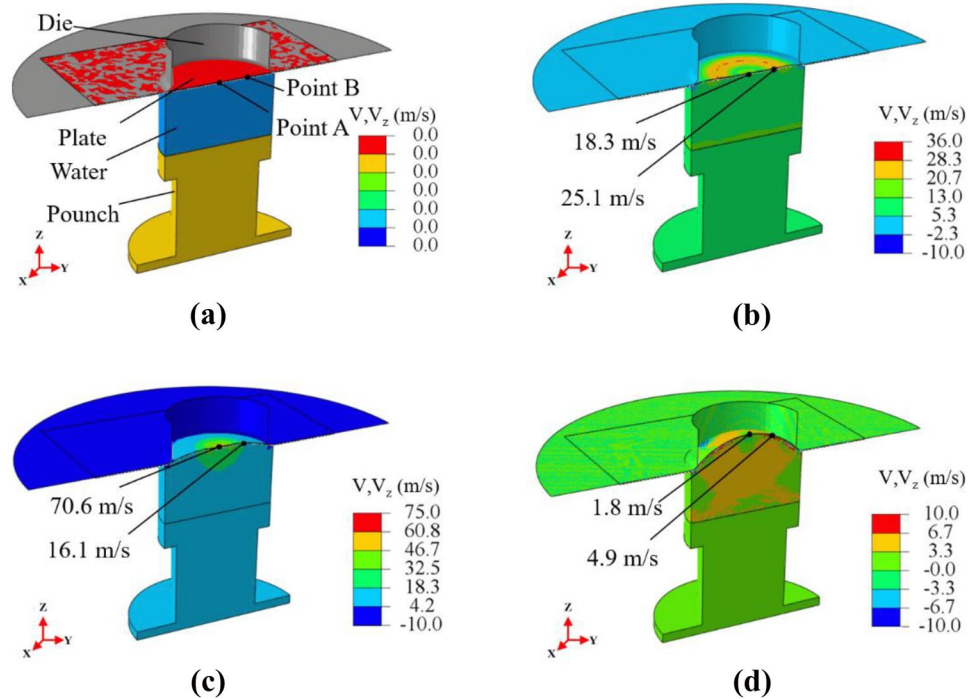


Figure 11 shows the thickness distribution of sheet after the EMF and EMHF processes, respectively. In both processes, the sheet center of is subjected to bidirectional isotensile stress; the thickness reduction is most obvious. In the EMF process, the center thickness of sheet is 0.37 mm

and the thinning rate is 26%. In EMHF, the center thickness of sheet is 0.33 mm and the thinning rate is 34%. The experimental and simulation results were consistent.

Figure 12 shows the variation in contact force on the sheet with time. Initially, no water pressure is generated on

Fig. 8 Deformation process in EMHF: (a) $t=0 \mu\text{s}$, (b) $t=220 \mu\text{s}$, (c) $t=430 \mu\text{s}$, and (d) $t=1200 \mu\text{s}$



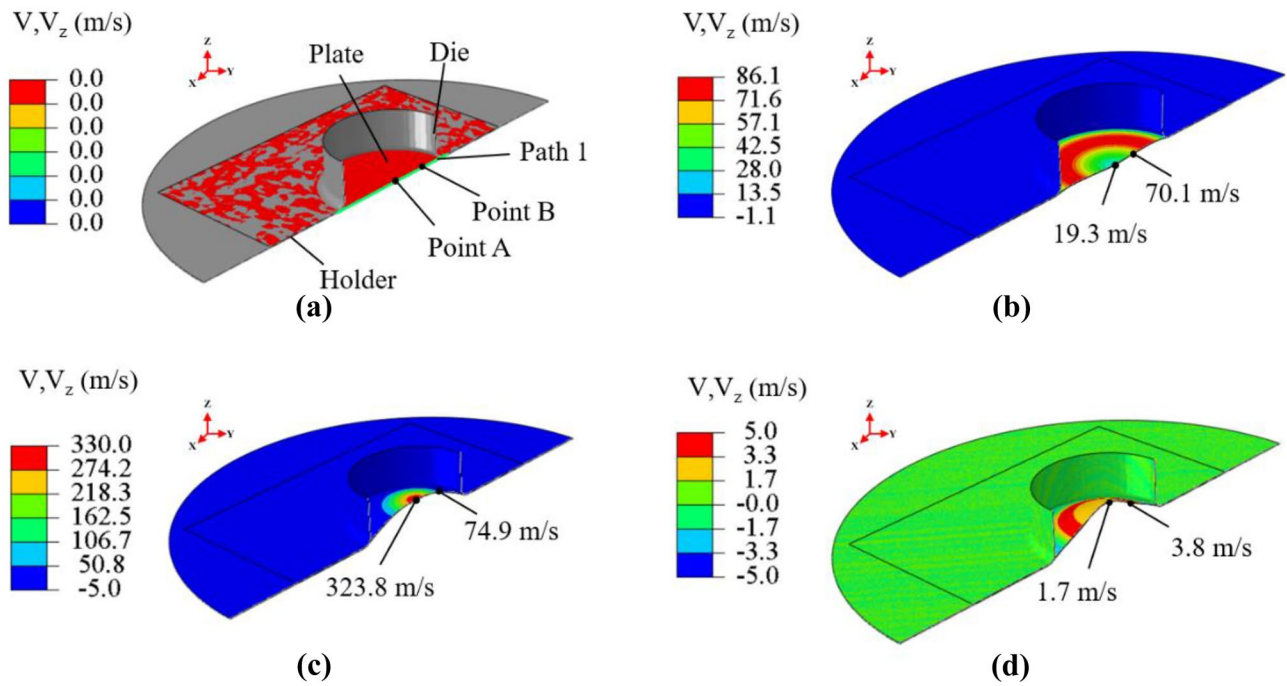


Fig. 9 Deformation process in EMF: (a) $t=0 \mu\text{s}$, (b) $t=60 \mu\text{s}$, (c) $t=135 \mu\text{s}$, and (d) $t=1000 \mu\text{s}$

sheet. At $220 \mu\text{s}$, the region of the sheet in contact with the die fillet is subjected to a larger contact force. At $430 \mu\text{s}$, there is no contact force in the center of the sheet. However, large contact forces are exerted on both sides of the sheet, acting in the direction perpendicular to the normal of the deformed sheet. A mixed region, containing both air and water, appears below the sheet center, as shown in Fig. 7c. Fluid in contact with the top of the sheet is air rather than water. Thus, no water pressure is imposed on sheet center at this time. At $1200 \mu\text{s}$, the water is in full contact with the sheet. The deformed sheet profile is finally uniform under the action of uniform contact pressure.

Figure 13a, b show the displacement curves of point A and point B with time during the EMF and EMHF processes, respectively. In EMF, the displacement of point B is always greater than the displacement of point A from 0 to $130 \mu\text{s}$. At $130 \mu\text{s}$, the displacement of point B is close to the maximum value, and the displacement with 10.5 mm of point B is the same with that of point A. After $130 \mu\text{s}$, the displacement of point A continues to increase under the action of the inertial force, and exceeds that of point B. When the deformation process ends, the displacement of points A and B are 19.1 mm and 11.3 mm , respectively. In EMF, the maximum equivalent plastic strain of point A and point B are 28% and

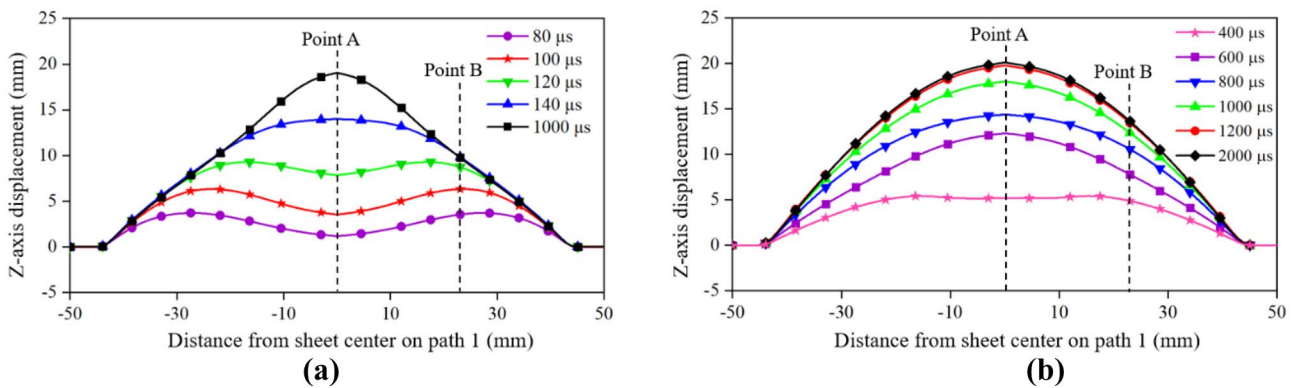


Fig. 10 Dynamic deformation process on Path 1: (a) EMF and (b) EMHF

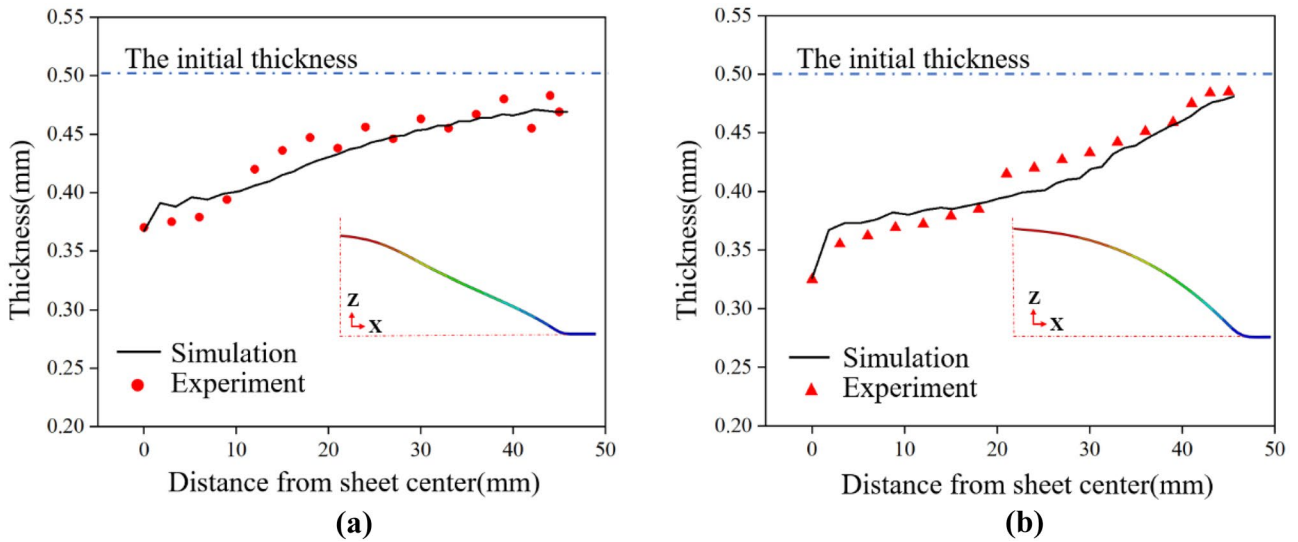
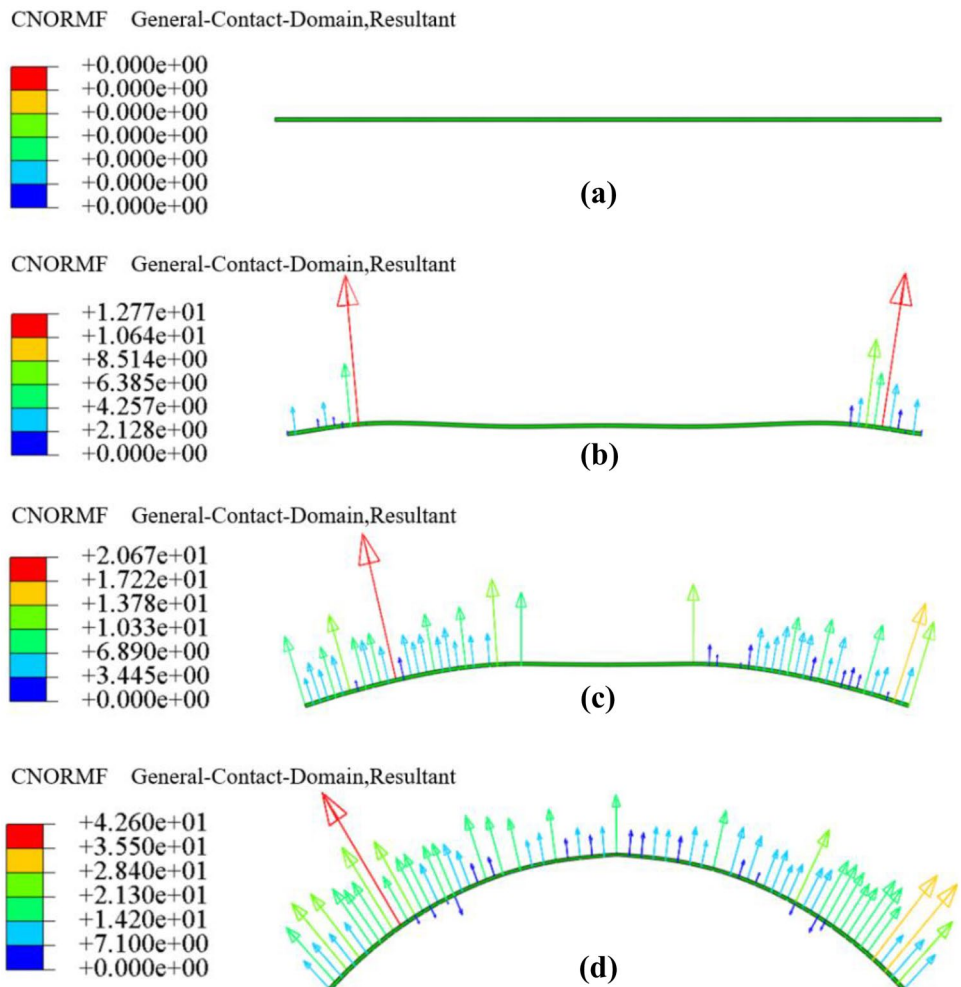


Fig. 11 Thickness distribution of the sheet: (a) EMF and (b) EMHF

14.1%, respectively. In EMHF, the displacement of point B and point A changes alternate in amplitude, switching between 0 and 400 μ s. At 400 μ s, the displacement with

5.2 mm of point B is the same with that of point A. After 400 μ s, the displacement of point A is larger than that of point B. In addition, the displacements of points A and point

Fig. 12 Contact force on sheet during EMHF: (a) $t=0 \mu$ s, (b) $t=220 \mu$ s, (c) $t=430 \mu$ s, and (d) $t=1200 \mu$ s



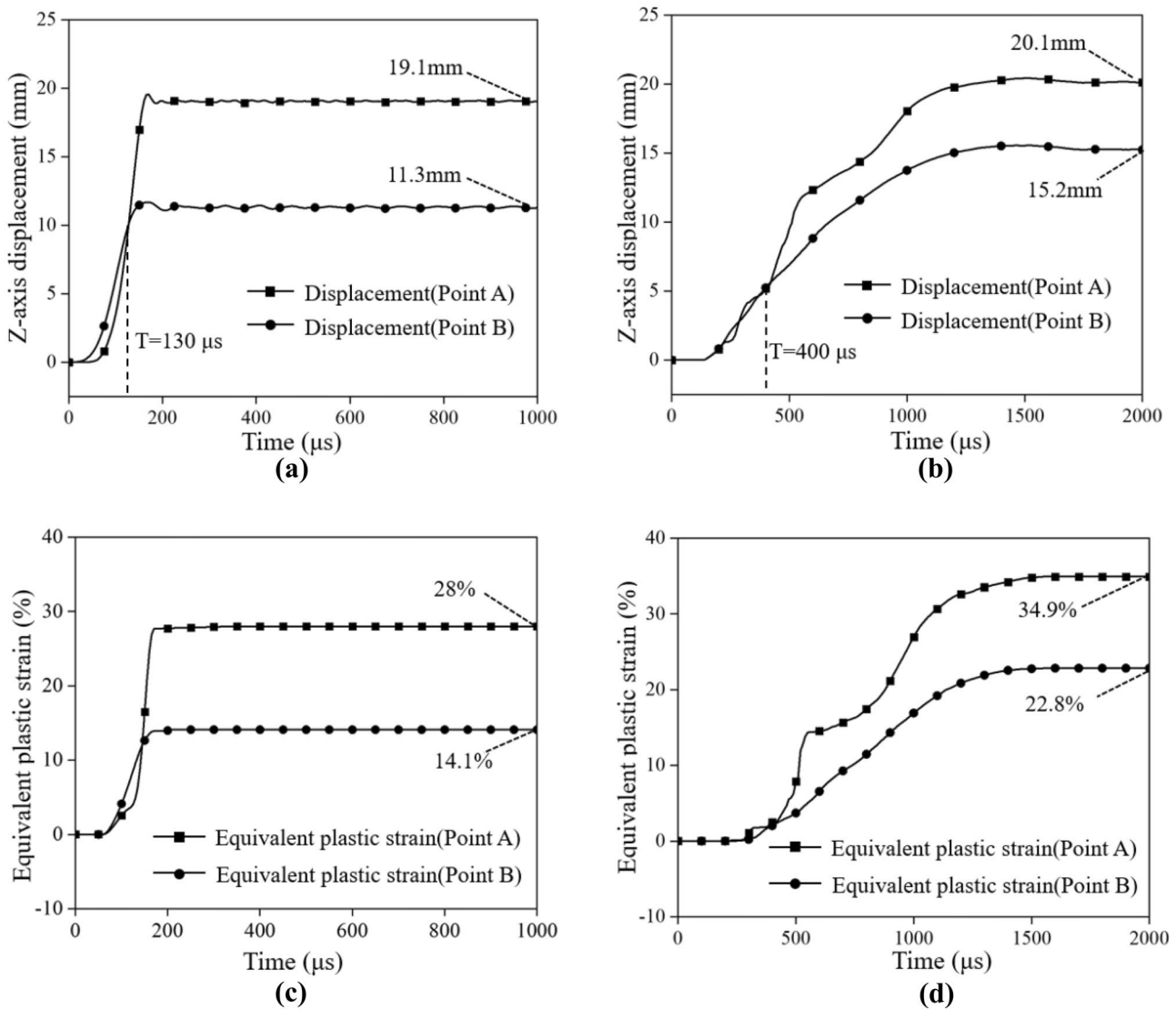


Fig. 13 Displacement and plastic strain at point A and point B: (a) displacement in EMF, (b) displacement in EMHF, (c) plastic strain in EMF, and (d) plastic strain in EMHF

B first increase with the time, then eventually remain stable. When the deformation ends, the displacement of points A and B are 20.1 mm and 15.2 mm, respectively. In EMHF, the maximum equivalent plastic strain of points A and B are 34.9% and 22.8%, respectively.

Figure 14 shows the changes in velocity and plastic strain rate at point A with time. In the EMF process, the velocity of point A reaches a maximum (323 m/s) at 135 μs , then rapidly decays. The plastic strain rate of point A reaches a peak (8456.8 s^{-1}) at 150 μs . In the EMHF process, the velocity of point A reaches a peak (70.6 m/s) at 430 μs and the plastic strain rate of point A reaches a peak (2176.8 s^{-1}) at 150 μs . Therefore, both EMF and EMHF are high-speed forming methods.

Figure 15 shows the distribution of three principal stresses and three principal strains at point A and point B

during the forming processes. The radial stresses are defined as σ_{r1} and σ_{r2} and stress along the material thickness direction is defined as σ_t . At point A, the maximum principal stress reaches a peak at 155 μs and the principal plastic strain reaches a maximum at the same time. Radial stresses σ_{r1} and σ_{r2} are 502.6 MPa and 493.4 MPa, respectively, and the first and second plastic strains are 13.6% and 13.5%, respectively. At point B, the maximum principal stress reaches a peak at 145 μs . Radial stresses σ_{r1} and σ_{r2} are 402.3 MPa and 270.9 MPa, respectively, and radial stress σ_{r1} is much greater than σ_{r2} . Thus, point A is in a state of bidirectional isotensile stress, whereas point B is in a state of bidirectional unequal tensile stress.

As shown in Fig. 16a, c, the maximum principal stress at point A reaches a maximum at 1020 μs , and radial stresses

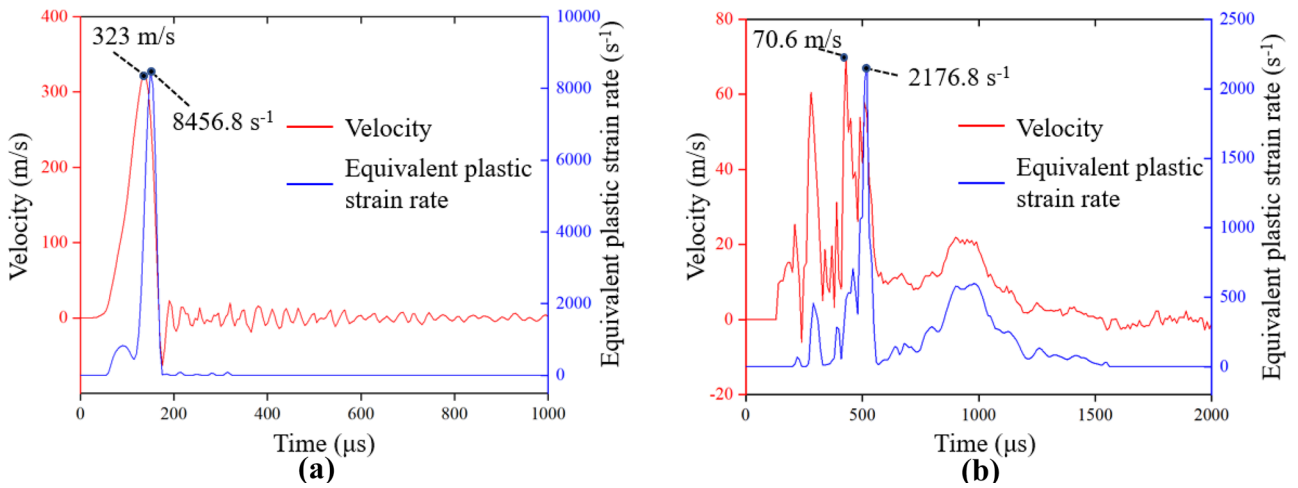


Fig. 14 Variation of velocity and plastic strain rate at point A with time: (a) EMF and (b) EMHF

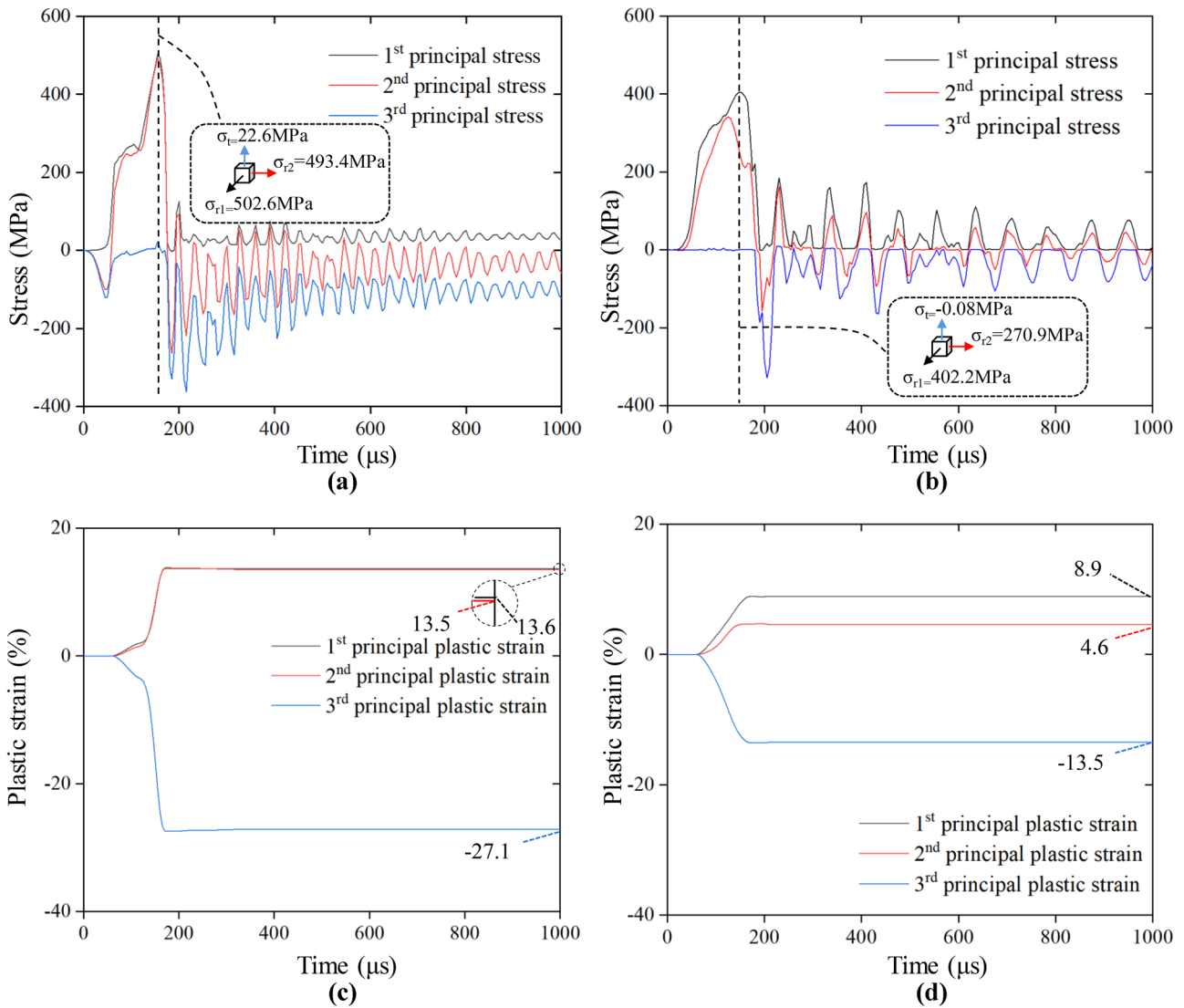


Fig. 15 Principal stresses and strains in EMF process: (a and c) point A and (b and d) point B

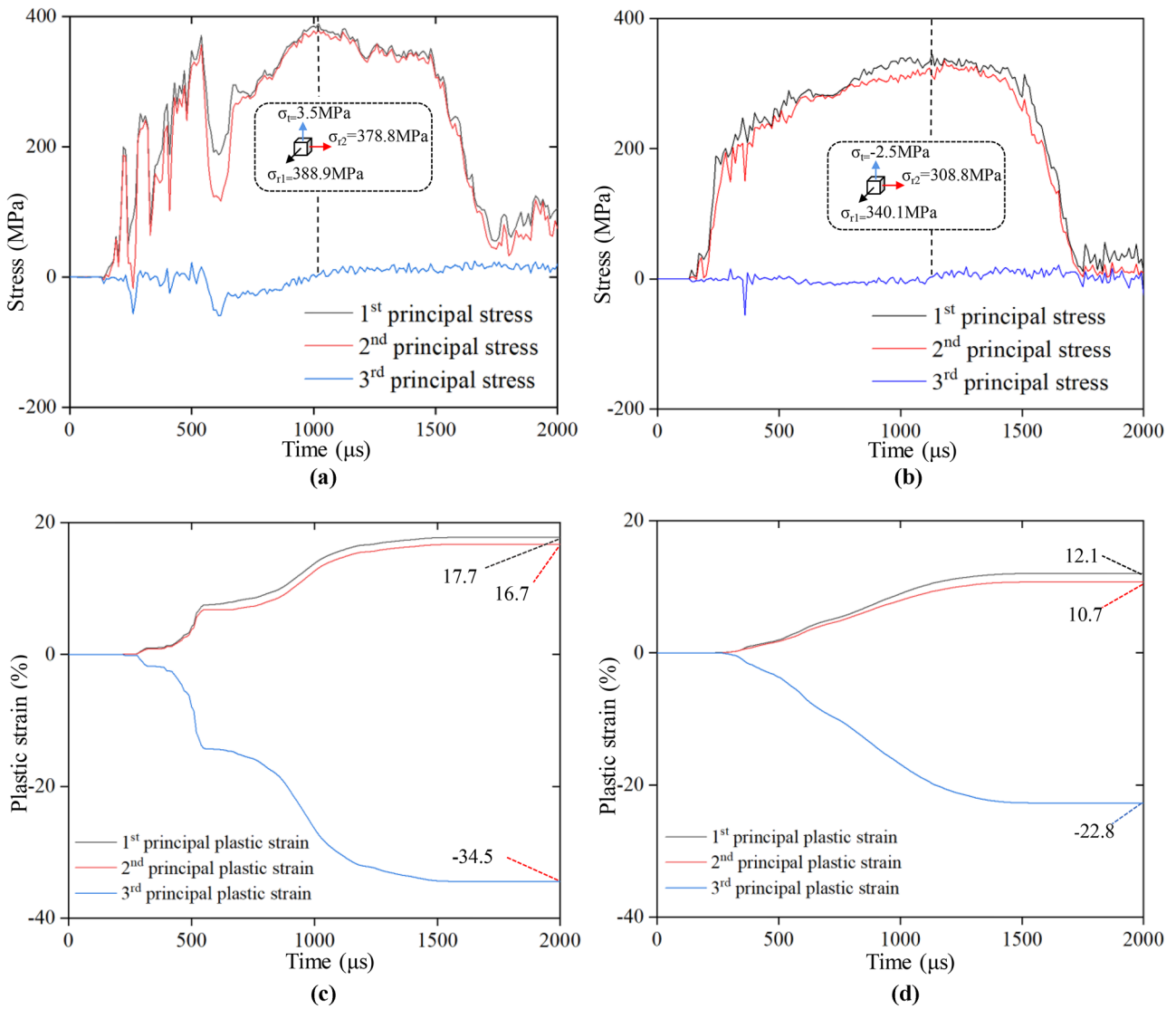


Fig. 16 Principal stress and strain in EMHF process: (a and c) point A and (b and d) point B

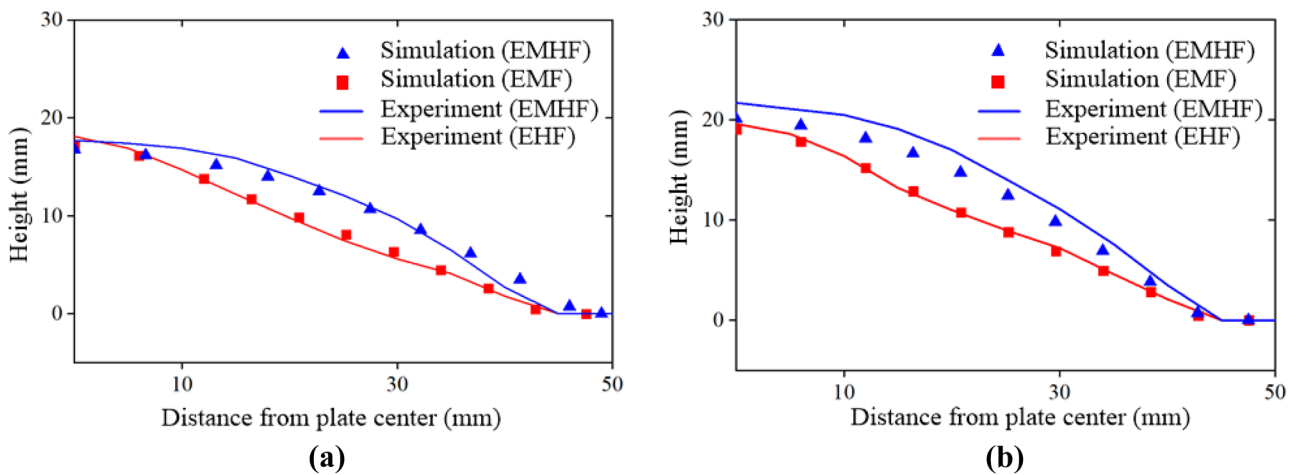


Fig. 17 Comparison of simulation and experimental results: (a) 4 kV and (b) 4.5 kV

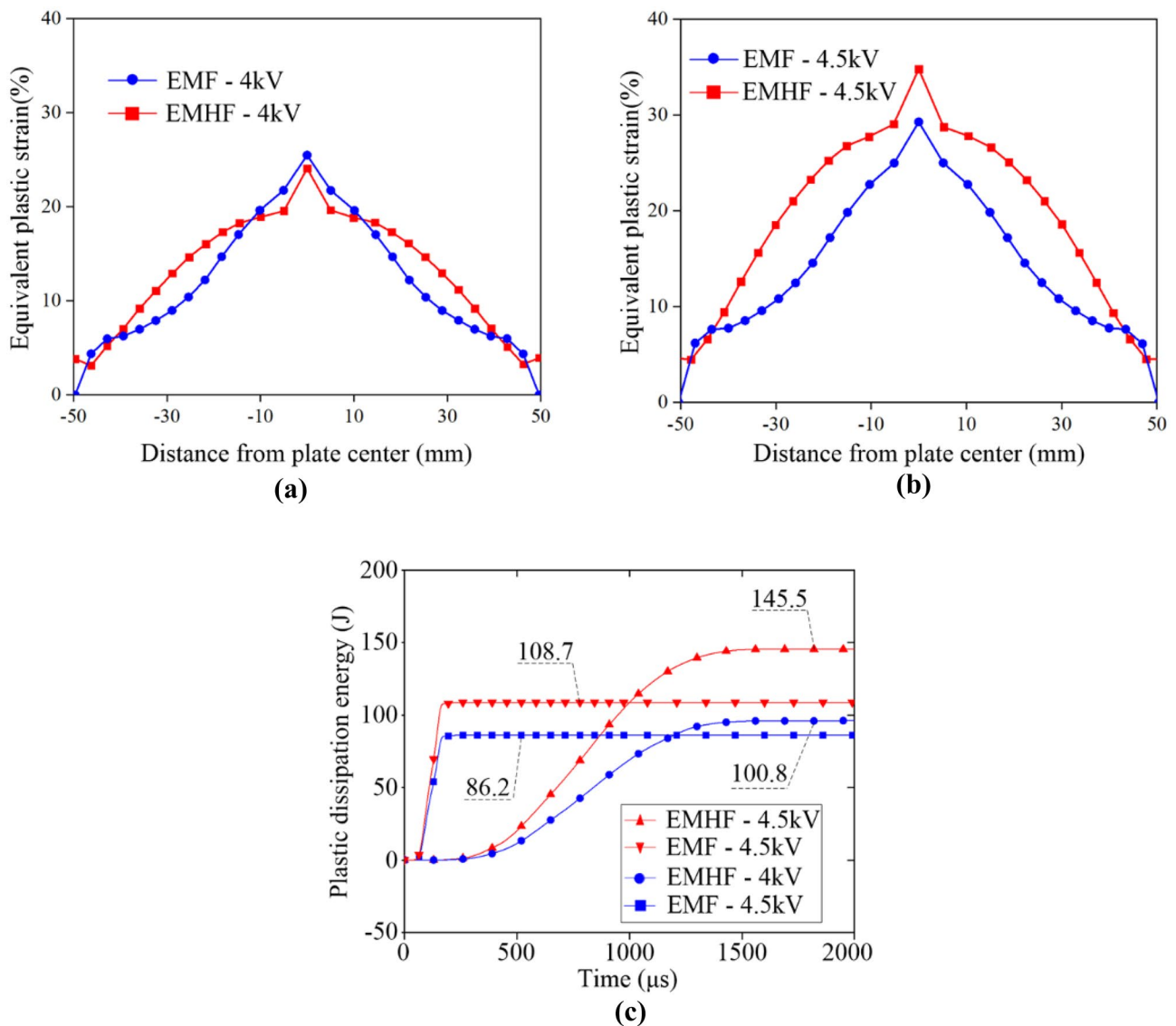


Fig. 18 Plastic strain and energy. (a) Equivalent plastic strain with 4 kV. (b) Equivalent plastic strain with 4.5 kV. (c) Change in plastic dissipation energy with time

σ_{r1} and σ_{r2} are 388.9 MPa and 377.8 MPa, respectively. However, the absolute value of the three-direction principal plastic strain is still increasing. At 2000 μs , the first and second principal plastic strains are 17.7% and 16.7%. At 1040 μs , radial stresses σ_{r1} and σ_{r2} at point B reach maximum values of 340.1 MPa and 308.8 MPa, respectively, and the first and second principal plastic strains are 12.1% and 10.7%, respectively. In EMHF, both point A and point B are close to a state of bidirectional isotensile stress.

Figure 17a, b show the experimental and simulation results at two different discharge voltages. The results are consistent. At a discharge voltage of 4 kV, the maximum error between the experimental and simulation results are 4.9% and 5.6% for EMF and EMHF, respectively. At a

discharge voltage of 4.5 kV, the maximum error are 4.1% and 7.4%, respectively. Thus, the numerical simulation method presented in this paper can be used to accurately analyze the dynamic deformation process in EMF and EMHF.

As shown in Fig. 18a, b, the deformation shape and equivalent plasticity of sheet were higher in EMHF than that in EMF. Therefore, the plastic dissipation energy of sheet in EMHF is larger than that in EMF. Figure 18c shows plastic energy dissipated during sheet deformation as a function of time. The same equipment was used in EMHF and EMF experiment. The maximum energy storage and capacitance of the EMF system are 200 kJ and 640 μF , respectively. The plastic energy dissipated in EMF and EMHF at a discharge voltage of 4 kV are 86.2 J and 100.8 J, respectively. The

plastic energy dissipated in EMF and EMHF at a discharge voltage of 4.5 kV are 108.7 J and 145.5 J, respectively. As the discharge voltage increases, the energy efficiency increases faster in EMHF compared with EMF.

4 Conclusions

The present work analyzed the dynamic deformation process of sheet in EMHF and EMF by numerical simulation and experimentally. The main results can be summarized as follows:

1. A three-dimensional finite element model was established to analyze the dynamic sheet deformation process in EMF and EMHF. Fluid–solid coupling and the effect of liquid compression on sheet deformation are considered in EMHF. The experimental and simulation results were consistent.
2. The deformed sheet profiles in EMF and EMHF are non-uniform conical and uniform semicircular, respectively. The magnetic field force is not evenly distributed on the sheet in the EMF process, whereas the liquid in EMHF can apply pressure more evenly on the surface of the workpiece.
3. When the discharge voltage is 4.5 kV, the maximum deformation velocity and strain rate are 70.6 m/s and 2176.8 s^{-1} , respectively. Thus, EMHF is a high-speed forming method.

Author contribution Peng Zhao: methodology, investigation, simulation, experiments, writing original draft. Xiaohui Cui: methodology, investigation, writing — review and editing. Ziqin Yan: investigation, collected data, experiments.

Funding This work was supported by the National Natural Science Foundation of China (Grant Numbers: 51775563 and 51405173), Innovation Driven Program of Central South University (Grant Number: 2019CX006), and the Project of State Key Laboratory of High Performance Complex Manufacturing, Central South University (ZZYJKT2020-02).

Availability of data and materials All data and materials are fully available without restriction.

Declarations

Ethical approval Not applicable.

Consent to participate Written informed consent for publication was obtained from all participants.

Consent to publish Written informed consent for publication was obtained from all participants.

Conflict of interest The authors declare no competing interests.

References

1. Su HL, Huang L, Li JJ, Xiao W, Zhu H, Feng F, Li HW, Yan SL (2021) Formability of AA 2219-O sheet under quasi-static, electromagnetic dynamic, and mechanical dynamic tensile loadings. *J Mater Sci Technol* 70:125–135
2. Li N, Yu HP, Xu Z, Fan ZS, Liu L (2016) Electromagnetic forming facilitates the transition of deformation mechanism in 5052 aluminum alloy. *Mater Sci Eng A* 673:222–232
3. Cui XH, Zhang ZW, Du ZH, Yu HL, Qiu DY, Cheng YQ, Xiao XT (2020) Inverse bending and springback-control using magnetic pulse forming. *J Mater Process Technol* 275:116374
4. Cui XH, Du ZH, Xiao A, Yan ZQ, Qiu DY, Yu HL, Chen BG (2021) Electromagnetic partitioning forming and springback control in the fabrication of curved parts. *J Mater Process Technol*. 288:116889
5. Du ZH, Yan ZQ, Cui XH, Chen BG, Yu HL, Qiu DY, Xia WZ, Deng ZS (2022) Springback control and large skin manufacturing by high-speed vibration using electromagnetic forming. *J Mat Process Technol* 299:117–340
6. Cui XH, Mo JH, Li JJ, Xiao XT (2017) Tube bulging process using multidirectional magnetic pressure. *Int J Adv Manuf Technol* 90:2075–2082
7. Yu HP, Chen J, Liu W, Yin HZ, Li CF (2018) Electromagnetic forming of aluminum circular tubes into square tubes: experiment and numerical simulation. *J Manuf Process* 31:613–623
8. Yan ZQ, Xiao A, Cui XH, Guo YZ, Lin YH, Zhang L, Zhao P (2021) Magnetic pulse welding of aluminum to steel tubes using a field-shaper with multiple seams. *J Manuf Process* 65:214–227
9. Cui XH, Mo JH, Zhu Y (2012) 3D modeling and deformation analysis for electromagnetic sheet forming process. *Trans Nonferrous Metals Soc China* 22:164–169
10. Xiong WR, Wang WP, Wan M, Li XJ (2015) Geometric issues in V-bending electromagnetic forming process of 2024–T3 aluminum alloy. *J Manuf Process* 19:171–182
11. Xu JR, Xie XY, Wen ZS, Cui JJ, Zhang X, Zhu DB, Liu Y (2019) Deformation behaviour of AZ31 magnesium alloy sheet hybrid actuating with Al driver sheet and temperature in magnetic pulse forming. *J Manuf Process* 37:402–412
12. Huang CQ, Liu HS, Cui XH, Xiao A, Long ZC, Yu HL (2021) Investigation of current-assisted electromagnetic tensile forming for sheet metal. *Int J Adv Manuf Technol*. <https://doi.org/10.1007/s00170-021-08025-y>
13. Vohnout VS (1998) A hybrid quasi-static/dynamic process for forming large sheet metal parts from aluminum alloys. Ph. D. thesis. The Ohio State University
14. Kiliclar Y, Demir OK, Engelhardt M, Rozgić M, Vladimirov IN, Wulfinghoff S, Weddeling C, Gies S, Klose C, Reese S, Tekkaya AE, Maier HJ, Stiemer M (2016) Experimental and numerical investigation of increased formability in combined quasi-static and high-speed forming processes. *J Mater Process Technol* 237:254–269
15. Liu DH, Li CF, Yu HP (2009) Numerical modeling and deformation analysis for electromagnetically assisted deep drawing of AA5052 sheet. *Trans Nonferrous Met Soc China* 19:1294–1302
16. Cui XH, Yu HL, Wang QS (2018) Reduction of corner radius of cylindrical parts by magnetic force under various loading methods. *Int J Adv Manuf Technol* 97:2667–2674
17. Feng F, Li JJ, Chen RC, Huang L (2021) Multi-point die electromagnetic incremental forming for large-sized sheet metals. *J Manuf Process* 62:458–470

Publisher's Note Springer Nature remains neutral with regard to jurisdictional claims in published maps and institutional affiliations.